arXiv:1704.04949v1 [cond-mat.quant-gas] 17 Apr 2017

Fingering instabilities and pattern formation in a two-component dipolar Bose-Einstein condensate

Kui-Tian Xi,[1,2,*] Tim Byrnes,[3,4,5,2,6] and Hiroki Saito[7]

[1]*Department of Physics, The Ohio State University, Columbus, Ohio 43210, USA*
[2]*New York University Shanghai, 1555 Century Avenue, Pudong, Shanghai 200122, China*
[3]*State Key Laboratory of Precision Spectroscopy, School of Physical and Material Sciences, East China Normal University, Shanghai 200062, China*
[4]*NYU-ECNU Institute of Physics at NYU Shanghai, 3663 Zhongshan Road North, Shanghai 200062, China*
[5]*National Institute of Informatics, 2-1-2 Hitotsubashi, Chiyoda-ku, Tokyo 101-8430, Japan*
[6]*Department of Physics, New York University, New York, NY 10003, USA*
[7]*Department of Engineering Science, University of Electro-Communications, Tokyo 182-8585, Japan*

(Dated: April 18, 2017)

We study fingering instabilities and pattern formation at the interface of an oppositely polarized two-component Bose-Einstein condensate with strong dipole-dipole interactions in three dimensions. It is shown that the rotational symmetry is spontaneously broken by fingering instability when the dipole-dipole interactions are strengthened. Frog-shaped and mushroom-shaped patterns emerge during the dynamics due to the dipolar interactions. We also demonstrate the spontaneous density modulation and domain growth of a two-component dipolar BEC in the dynamics. The corresponding Bogoliubov analyses in the two-dimensional approximation are performed, and the characteristic lengths of the domains are estimated analytically. Patterns in resemblance to that in the magnetic classical fluids are modulated when the number ratio of atoms, trap ratio of external potential, or tilted polarization with respect to z direction are varied.

I. INTRODUCTION

Fingering instabilities (e.g., Saffman-Taylor instability and Rayleigh-Taylor instability) lead to complicated pattern formation of an interface [1, 2], and ubiquitously occurs at the interface between two fluids of different densities and viscosities, such as water suspended atop oil in gravity [3], Hele-Shaw cell between two plates [4–6], biological systems [7], mushroom clouds from volcanic eruptions and nuclear explosions in the atmosphere, plasma fusion [8, 9], supernova explosions [10, 11], and the Crab Nebula [12]. In addition, domains of magnetic fluids are also known to undergo fingering instability and form complex labyrinthine patterns [13, 14].

In resemblance to the classical fluids, a system of two superfluids can also exhibit a Rayleigh-Taylor interfacial instability, for instance, a system of a two-component Bose-Einstein condensate (BEC) [15–19]. What is more, a two-component BEC of an atomic gas with strong dipole-dipole interactions (DDI) exhibits similarities with those in classical magnetic fluids, such as hexagonal, solitonlike, and labyrinthine pattern formation [20].

Recently, a dipolar BEC with strong DDI was shown to exhibit self-organized crystallization, which is observed in the quench dynamics [21], and leads to novel self-bound droplet states of superfluid [22, 23]. These emerging phenomena have inspired many theoretical studies to clarify the implicit new physics behind stabilization against collapse and droplet pattern formation [24–31].

In this paper, we consider a two-component BEC with strong DDI in which the dipole moments of the two components are polarized oppositely. By modulating the strength of DDI, we demonstrate that spontaneous symmetry breaking is induced in the form of fingering instabilities occurring at the interface between the two components, which leads to typical frog-shaped and mushroom-shaped pattern formation. The Bogoliubov dispersion relation corresponding to the fingering instability is analyzed in the two-dimensional approximation. Spontaneous density modulation and domain growth are also shown as time evolves in the dynamics, along with analytical estimations of the characteristic lengths of the dipolar domains. Droplet patterns are formed when the population imbalance in two components becomes large; a labyrinthine pattern grows as the trap ratio increases; a stripe phase occurs as the tilted angle increases.

This paper is organized as follows. In Sec. II, we describe precisely the problem statement. In Sec. III, we demonstrates the symmetry-breaking fingering instability (Sec. III A) and domain dynamics of the system (Sec. III B), in which the Bogoliubov analyses and the estimations of characteristic lengths of the dipolar domain are performed. In Sec. IV, we show the stationary pattern formation as number ratio of atoms (Sec. IV A), trap ratio (Sec. IV B), and tilted polarization (Sec. IV C) are varied. In Sec. V, we give the conclusions of our study.

II. FORMULATION OF THE PROBLEM

A two-component BEC with DDI at zero temperature is described by the macroscopic wave functions $\Psi_1(\boldsymbol{r},t)$ and $\Psi_2(\boldsymbol{r},t)$ in the mean-field regime, which obey the nonlocal Gross-Pitaevskii (GP) equations given by

$$i\hbar\frac{\partial}{\partial t}\Psi_i(\boldsymbol{r}) = \Bigg[-\frac{\hbar^2}{2m_i}\nabla^2 + V(\boldsymbol{r}) + \sum_{j=1}^{2} g_{ij}\left|\Psi_j(\boldsymbol{r})\right|^2 + \sum_{j=1}^{2}\int U_{ij}(\boldsymbol{r}-\boldsymbol{r}')\left|\Psi_j(\boldsymbol{r}')\right|^2 d\boldsymbol{r}'\Bigg]\Psi_i(\boldsymbol{r}), \quad (1)$$

* xi.99@osu.edu; kuitian.xi@nyu.edu

where m_i is the atomic mass for component i ($i = 1, 2$). The two-body coupling constants are $g_{ij} = 2\pi\hbar^2 a_{ij}/m_{ij}$ with a_{ij} and m_{ij} being the s-wave scattering length and the reduced mass between components i and j, respectively. The macroscopic wave function Ψ_i is normalized as $\int |\Psi_i|^2 d\boldsymbol{r} = N_i$, where N_i is the number of atoms in component i. The DDI has the form

$$U_{ij}(\boldsymbol{r}) = \frac{\mu_0 \mu_i \mu_j \left(1 - 3\cos^2\theta\right)}{4\pi r^3}, \tag{2}$$

where μ_0 is the magnetic permeability of vacuum, μ_i is the magnetic dipole moment of component i, and θ is the angle between the direction of polarization and $\boldsymbol{r}$. In our calculations, the masses of the two components are assumed to be the same, i.e., $m_1 = m_2 = m$, and the atoms are trapped in the same axisymmetric harmonic potential $V = m[\omega_\perp^2(x^2 + y^2) + \omega_z z^2]/2$, where $\omega_\perp$ and ω_z are the radial and axial trap frequencies, respectively.

In our numerical simulations, we solve the three-dimensional nonlocal GP equations Eq. (1) using pseudospetral method with a fast Fourier transform, where the dipolar interaction terms Eq. (2) are calculated using convolution theorem. We take ^{52}Cr as the atoms in the two-component system, with $\mu_1 = 6\mu_B$ and $\mu_2 = -6\mu_B$. Experimentally, such a two-component dipolar BEC system can be implemented by using $^7S_3$ $m_J = -3$ and $+3$ states of ^{52}Cr [32, 33], and the s-wave scattering lengths a_{ij} can be modulated by using Feshbach resonance [34].

III. INSTABILITIES AND DYNAMICS

A. Fingering Instabilities

We now investigate the fingering instabilities at the interface between two components with different strengths of dipolar interactions. For convenience, we introduce the strength coefficient γ of the DDI as

$$U_{ij}(\boldsymbol{r}) = \gamma \frac{\mu_0 \mu_i \mu_j \left(1 - 3\cos^2\theta\right)}{4\pi r^3}. \tag{3}$$

Experimentally, the coefficient γ can be tuned by fast rotation of the magnetic field [35]. We initially prepare stationary states without dipolar interactions, which are matastable states with unstable interfaces. The dipolar interactions are then suddenly introduced at $t = 0$, followed by time evolution. The parameters are taken to be $a_{11} = 100a_B$, $a_{22} = 1.1a_{11}$, $a_{12} = 1.2a_{11}$, $(\omega_\perp, \omega_z) = 2\pi \times (100, 800)$ Hz, and $N_1 = 1 \times 10^6$, $N_2 = 2 \times 10^6$. The scattering lengths satisfy the phase-separation condition, $g_{11}g_{22} < g_{12}g_{21}$, and the ground state without DDI has a circular interface between the two components.

The column density profiles, obtained by the integration of the densities along the z direction, are shown in Fig. 1 and Fig. 2, in which $\gamma = 0.18$ and 1, respectively. In the absence of dipolar interactions, the immiscible states of the two components exhibit rotational symmetry as expected, which are shown in Fig. 1(a) and Fig. 2(a). As the dipolar interactions are induced, the rotational symmetry of the circular interface is spontaneously broken, leading to a fingering instability at the interface between the two components, which is similar to the interface behavior of classical dipolar fluids [14]. With smaller dipolar interactions, the system exhibits spontaneous rotational symmetry breaking with smaller length scales, comparing Fig. 1 with Fig. 2. For $\gamma = 0.18$, a frog-shaped pattern occurs in component 1 at $t = 100$ ms, as shown in Fig. 1(g). For $\gamma = 1$, a mushroom-shaped pattern appears at the interface at $t = 6$ ms, as shown in Fig. 2(c). At $t = 7$ ms with $\gamma = 1$, the whole interface of two components explodes into a fully mushroom-shaped pattern. It is shown that with stronger dipolar interactions, the interface of a two-component BEC becomes more unstable.

For comparison, we then investigate the case in the absence of DDI, in which the scattering lengths are suddenly changed from immiscible to miscible, $g_{11}g_{22} > g_{12}g_{21}$ at $t = 0$. As shown in Fig. 3, no fingering instability occurs at the interface without DDI, and the initially phase-separated two components mix in the dynamics, which demonstrates that the immiscible-miscible transition has no contribution to the fingering instability at the interface. These results reveal that with strong dipolar interactions, the interface instability patterns can also emerge in the superfluids much like those in classical fluids. Three movies [36–38] show the time evolution of the column densities of two components with $\gamma = 0.18$ and 1, as well as that with $\gamma = 0$.

For a deeper understanding of the instability, we perform a Bogoliubov analysis for the system. To simplify the calculation, the dimensionality of the system is reduced to two dimensions (2D). We assume that the z dependence of the wave function is decomposed as

$$\Psi_i(\boldsymbol{r}, t) = \psi_i(\boldsymbol{\rho}, t) \frac{1}{\left(\pi\zeta^2\right)^{1/4}} e^{-z^2/(2\zeta^2)}, \tag{4}$$

where $\boldsymbol{\rho} = (x, y)$ and ζ is the width of density profile in the z direction. The value of ζ is determined by fitting the Gaussian to the numerically obtained wave function. Eq. (1) is then rewritten as

$$i\hbar\frac{\partial}{\partial t}\psi_i = \Bigg[-\frac{\hbar^2}{2m_i}\nabla_{\boldsymbol{\rho}}^2 + V(\boldsymbol{\rho}) + \sum_{j=1}^{2} g_{ij}^{2D}\left|\psi_j\right|^2 + \sum_{j=1}^{2}\int U_{ij}^{2D}(\boldsymbol{\rho} - \boldsymbol{\rho}')\left|\psi_j(\boldsymbol{\rho}')\right|^2 d\boldsymbol{\rho}' \Bigg]\psi_i, \tag{5}$$

where $V(\rho) = m\omega_\perp^2(x^2 + y^2)/2$ and $g_{ij}^{2D} = g_{ij}/\sqrt{2\pi\zeta^2}$. The 2D dipolar interaction reads [39]

$$U_{ij}^{2D}(\boldsymbol{\rho} - \boldsymbol{\rho}') = \frac{\mu_0 \mu_i \mu_j}{3\sqrt{2\pi\zeta^2}} \int \frac{d\boldsymbol{k}}{(2\pi)^2} e^{-i\boldsymbol{k}\cdot(\boldsymbol{\rho} - \boldsymbol{\rho}')} h(q), \tag{6}$$

where the dipolar kernel $h(q) = 2 - 3\sqrt{\pi} q e^{q^2} \mathrm{erfc}(q)$ with $q = k\zeta/\sqrt{2}$ for polarized spins in the z direction.

Define $\phi_i(\rho)$ as the stationary state with rotational symmetry, then weak perturbations of the wave functions can be

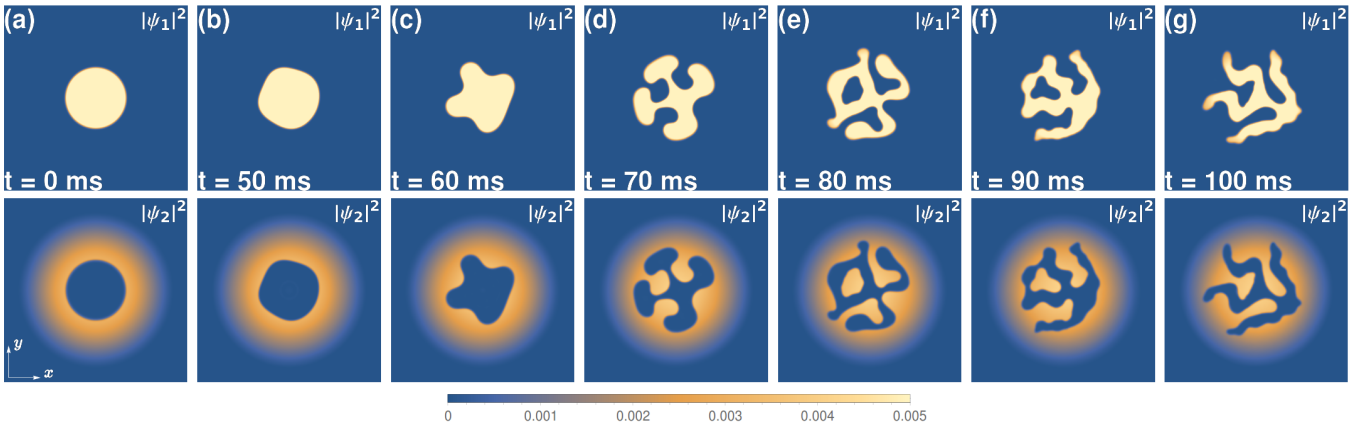

FIG. 1. (Color online) Column density profiles $|\psi_1|^2 = \int |\Psi_1|^2 dz$ and $|\psi_2|^2 = \int |\Psi_2|^2 dz$ for dynamical states of $\gamma = 0.18$ starting with non-dipolar stationary states. $a_{11} = 100a_B$, $a_{22} = 1.1a_{11}$, $a_{12} = 1.2a_{11}$, $(\omega_\perp, \omega_z) = 2\pi \times (100, 800)$ Hz, $N_1 = 1 \times 10^6$, $N_2 = 2 \times 10^6$. $\mu_1 = 6\mu_B$, $\mu_2 = -6\mu_B$. (a) - (g): $t = 0$, 50, 60, 70, 80, 90, and 100 ms, respectively. The top row is for component 1, while the bottom row is for component 2. The field of view is 56×56 μm. See Supplemental Material for the movie of the dynamics [36].

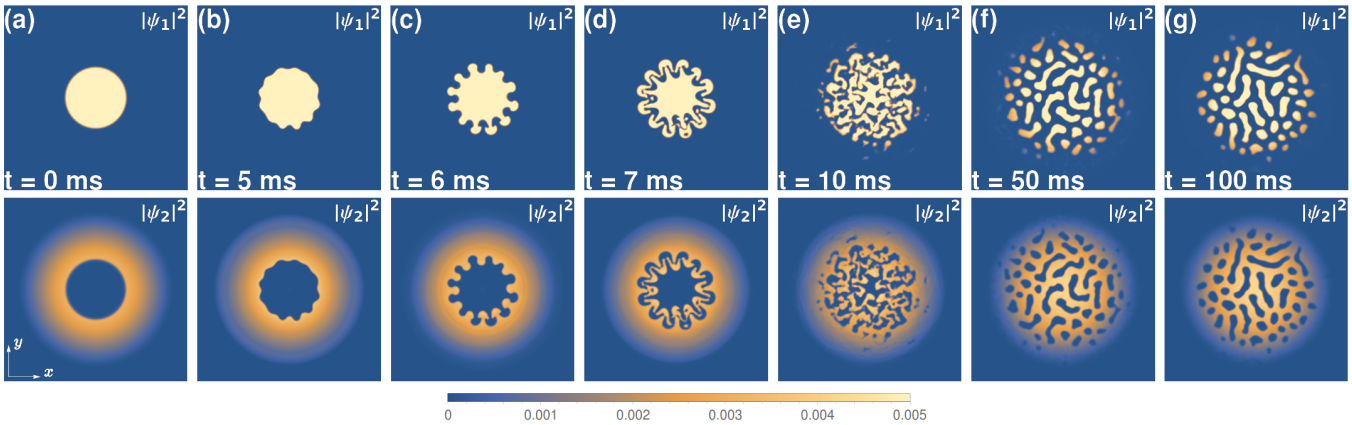

FIG. 2. (Color online) Column density profiles $|\psi_1|^2 = \int |\Psi_1|^2 dz$ and $|\psi_2|^2 = \int |\Psi_2|^2 dz$ for dynamical states of $\gamma = 1$ starting with non-dipolar stationary states. $a_{11} = 100a_B$, $a_{22} = 1.1a_{11}$, $a_{12} = 1.2a_{11}$, $(\omega_\perp, \omega_z) = 2\pi \times (100, 800)$ Hz, $N_1 = 1 \times 10^6$, $N_2 = 2 \times 10^6$. $\mu_1 = 6\mu_B$, $\mu_2 = -6\mu_B$. (a) - (g): $t = 0$, 5, 6, 7, 10, 50, and 100 ms, respectively. The top row is for component 1, while the bottom row is for component 2. The field of view is 56×56 μm. See Supplemental Material for the movie of the dynamics [37].

expressed as,

$$\psi_i(\boldsymbol{\rho}, t) = e^{-iM_i t/\hbar}\Big[\phi_i(\rho) + u_i(\rho)\, e^{iL\varphi} e^{-i\Omega t} + v_i^*(\rho)\, e^{-iL\varphi} e^{i\Omega^* t}\Big], \tag{7}$$

where M_i is the chemical potential of component i, the amplitudes $u_i(\rho)$ and $v_i(\rho)$ are treated as small, $\varphi = \tan^{-1}(y/x)$, and Ω is the frequency of the oscillation. The quantum number L characterizes the angular momentum of the modes.

Substituting Eq. (7) into Eq. (5), and collecting the first order terms proportional separately to $e^{\pm i\Omega t}$, then we obtain the following Bogoliubov de Gennes (BdG) equations,

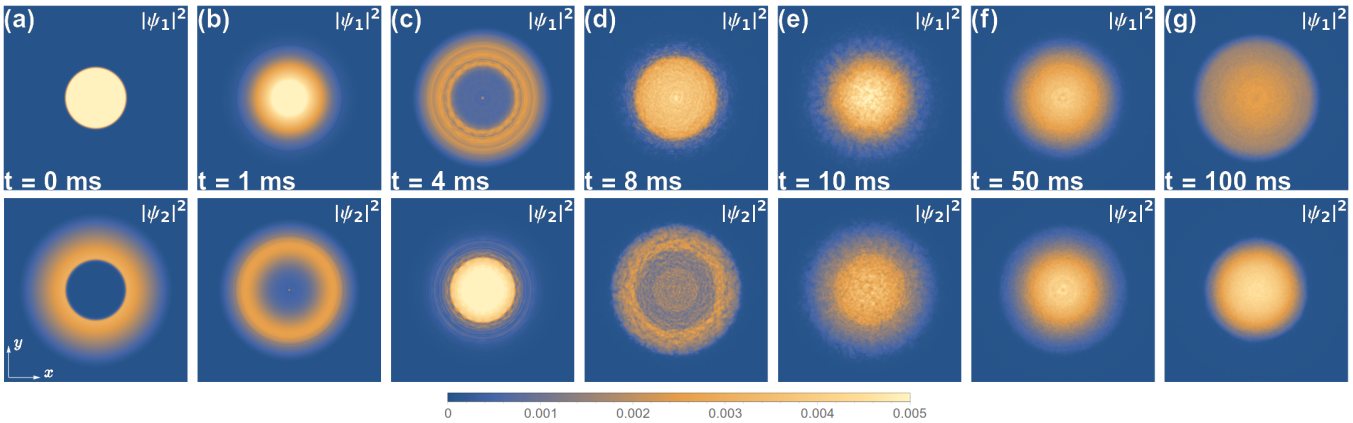

FIG. 3. (Color online) Column density profiles $|\psi_1|^2 = \int |\Psi_1|^2 dz$ and $|\psi_2|^2 = \int |\Psi_2|^2 dz$ for dynamical states of $\gamma = 0$ starting with non-dipolar stationary states. $a_{11} = a_{22} = 100a_B$, $a_{12} = 0.5a_{11}$, $(\omega_\perp, \omega_z) = 2\pi \times (100, 800)$ Hz, $N_1 = 1 \times 10^6$ and $N_2 = 2 \times 10^6$. (a) - (g): $t = 0$, 5, 6, 7, 10, 50, and 100 ms, respectively. The top row is for component 1, while the bottom row is for component 2. The field of view is 56×56 μm. See Supplemental Material for the movie of the dynamics [38].

$$\begin{aligned}
\Omega u_i = &\left(H_0 - M_i\right)u_i + \left(2g_{ii}^{2D}\left|\phi_i\right|^2 + g_{ij}^{2D}\left|\phi_j\right|^2\right)u_i + g_{ii}^{2D}\phi_i^2 v_i + g_{ij}^{2D}\left(\phi_j^*\phi_i u_j + \phi_j\phi_i v_j\right) \\
&+ \int d\boldsymbol{\rho}' \left[U_{ii}^{2D}\left|\phi_i(\rho')\right|^2 + U_{ij}^{2D}\left|\phi_j(\rho')\right|^2\right]u_i + \int d\boldsymbol{\rho}' U_{ii}^{2D}\left[\phi_i^*(\rho')\phi_i(\rho)u_i(\rho') + \phi_i(\rho')\phi_i(\rho)v_i(\rho')\right]e^{iL\varphi'} \\
&+ \int d\boldsymbol{\rho}' U_{ij}^{2D}\left[\phi_j^*(\rho')\phi_i(\rho)u_j(\rho') + \phi_j(\rho')\phi_i(\rho)v_j(\rho')\right]e^{iL\varphi'}, \qquad (8) \\
-\Omega v_i = &\left(H_0 - M_i\right)v_i + \left(2g_{ii}^{2D}\left|\phi_i\right|^2 + g_{ij}^{2D}\left|\phi_j\right|^2\right)v_i + g_{ii}^{2D}\phi_i^{*2}u_i + g_{ij}^{2D}\left(\phi_j\phi_i^* v_j + \phi_j^*\phi_i^* u_j\right) \\
&+ \int d\boldsymbol{\rho}' \left[U_{ii}^{2D}\left|\phi_i(\rho')\right|^2 + U_{ij}^{2D}\left|\phi_j(\rho')\right|^2\right]v_i + \int d\boldsymbol{\rho}' U_{ii}^{2D}\left[\phi_i(\rho')\phi_i^*(\rho)v_i(\rho') + \phi_i^*(\rho)\phi_i^*(\rho')u_i(\rho')\right]e^{iL\varphi'} \\
&+ \int d\boldsymbol{\rho}' U_{ij}^{2D}\left[\phi_j(\rho')\phi_i^*(\rho)v_j(\rho') + \phi_j^*(\rho')\phi_i^*(\rho)u_j(\rho')\right]e^{iL\varphi'}, \qquad (9)
\end{aligned}$$

where $H_0 = -\hbar^2\nabla^2/(2m) + V(\rho)$, and $i, j = 1, 2$.

We numerically diagonalize Eqs. (8) and (9) to study the instability of the system. If Ω has a positive imaginary part, the system exhibits a dynamical instability, and the unstable modes will grow exponentially to the evolution limitation arising from the nonlinearities. The imaginary part of the Bogoliubov excitation frequency Im[Ω] as a function of dipolar strength coefficient γ is shown in Fig. 4 with modes $L = 2$ to 10, among which the modes with the largest Im[Ω] dominate the instability dynamics. For the $L = 0$ and 1 modes (monopole and dipole modes), Im[Ω] = 0 and these modes are stable. Each mode in $L = 2$ to 10 has its critical strength of dipolar interaction, above which Im[Ω] > 0 and monotonically rises. When $\gamma = 0.18$ (the vertical black dashed line in Fig. 4) corresponding to Fig. 1, the interface is unstable with modes $L = 3$ to 6, in which the modes of $L = 4$ and 5 with the relatively largest Im[Ω] are predominant in the instability dynamics. Therefore, the results shown in Fig. 1 are in agreement with the Bogoliubov analysis.

We then analyze the fingering instability at the interface induced by the DDI. The DDI energy of the system in the 2D approximation is given by

$$\begin{aligned}
E_{dd} = &\frac{g_{dd}}{2}\int d\boldsymbol{\rho} d\boldsymbol{\rho}' \int \frac{d\boldsymbol{k}}{(2\pi)^2} e^{-i\boldsymbol{k}\cdot(\boldsymbol{\rho}-\boldsymbol{\rho}')} h(q) \\
&\times \left[n_1(\boldsymbol{\rho}) - n_2(\boldsymbol{\rho})\right]\left[n_1(\boldsymbol{\rho}') - n_2(\boldsymbol{\rho}')\right], \qquad (10)
\end{aligned}$$

where $g_{dd} = \mu_0(6\mu_B)^2/\left(3\sqrt{2\pi\zeta^2}\right)$, and $n_i = |\psi_i|^2$ is the 2D density for component i. For simplicity, we assume that components 1 and 2 have uniform distributions in $y \lesssim 0$ and $y \gtrsim 0$, respectively. The interface is located at $y \simeq 0$, and the position of the interface is defined by

$$y = \eta(x, t). \qquad (11)$$

A smoothed step function is introduced as

$$f(y) = \begin{cases} 0 & \text{if } y \to -\infty; \\ 1 & \text{if } y \to +\infty, \end{cases} \qquad (12)$$

and $f'(y) > 0$ is localized at $y \simeq 0$. Using Eqs. (11) and (12), the densities of the two components can be expressed as

$$n_1(\boldsymbol{\rho}, t) = n_1^0 f\left[-y + \eta(x, t)\right], \qquad (13)$$

$$n_2(\boldsymbol{\rho}, t) = n_2^0 f\left[y - \eta(x, t)\right]. \qquad (14)$$

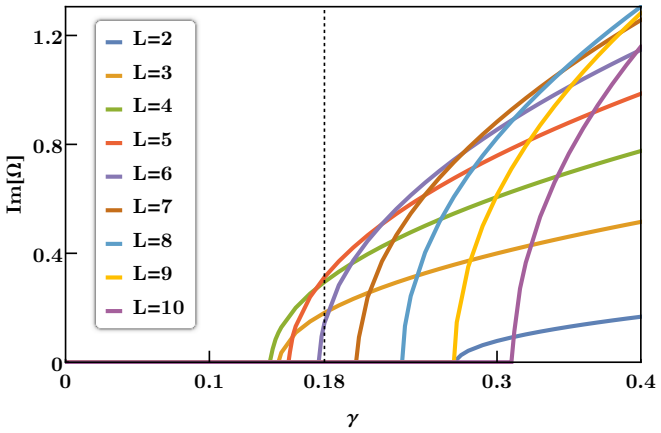

FIG. 4. (Color online) Imaginary part of Bogoliubov excitation frequency Im[Ω] as a function of γ. The modes for $2 \le L \le 10$ are plotted, while Im[Ω] = 0 for the $L = 0$ and 1 modes. The vertical black dashed line indicates $\gamma = 0.18$, corresponding to the parameter in Fig. 1.

We assume that η is small and the densities can be expanded as

$$n_1(\boldsymbol{\rho}, t) = n_1^0 f(-y) + n_1^0 f'(y)\eta(x,t), \tag{15}$$

$$n_2(\boldsymbol{\rho}, t) = n_2^0 f(y) - n_2^0 f'(y)\eta(x,t), \tag{16}$$

where we assume $f'(-y) = f'(y)$. By neglecting the terms that are independent of η, we obtain the pressure difference at the interface as the following,

$$\frac{\delta E_{dd}}{\delta\eta(x,t)} = g_{dd}\left(n_1^0 + n_2^0\right)^2 \int dx' \int \frac{d\boldsymbol{k}}{(2\pi)^2} e^{-ik_x(x'-x)} \times h(q)\, g^2(k_y)\, \eta(x',t), \tag{17}$$

where

$$g(k_y) = \int dy f'(y)\, e^{-ik_y y}. \tag{18}$$

The function $f'(y)$ is assumed to be Gaussian,

$$f'(y) = \frac{e^{-y^2/l_y^2}}{\sqrt{\pi} l_y}, \tag{19}$$

which gives

$$g(k_y) = e^{-k_y^2 l_y^2/4}. \tag{20}$$

Assuming that $\eta(x,t) \propto \sin(\kappa x - \varpi t)$, we obtain

$$\frac{\delta E_{dd}}{\delta\eta(x,t)} = g_{dd}\left(n_1^0 + n_2^0\right)^2 \eta(x,t) \times \int \frac{dk_y}{2\pi} h\left(\frac{l_z}{\sqrt{2}}\sqrt{\kappa^2 + k_y^2}\right) g^2(k_y) \tag{21}$$

$$\equiv F(\kappa)\,\eta(x,t). \tag{22}$$

Eq. (22) is similar to the form in the Rayleigh-Taylor instability of classical fluids, in which $F(\kappa)$ plays a role of the gravitational force in resemblance to that in the classical fluids [1, 2]. Thus, according to the Rayleigh-Taylor dispersion relation of the interface mode [40], we obtain

$$\varpi = \sqrt{\frac{F(\kappa)\kappa + \sigma\kappa^3}{m\left(n_1^0 + n_2^0\right)}}, \tag{23}$$

where σ is the 2D interface tension coefficient. When $F(\kappa)\kappa + \sigma\kappa^3 < 0$, the interface mode with wave number κ is dynamically unstable. Using the parameters in Fig. 1, where the numerically obtained interface profile is fitted to Eq. (19) and the interface tension coefficient in Ref. [41] is employed, the most unstable wavelength $2\pi/\kappa$ is estimated to be $\simeq 7\,\mu$m, which is in qualitative agreement with that in Fig. 1. For more accurate estimation of the unstable wave number, we must consider the circular geometry of the system. Moreover, the interface tension is modified by the DDI, which should be taken into account.

B. Domain Dynamics

We now investigate the domain dynamics for another initial condition. The initial state is the stationary state Ψ_0 of a single-component dipolar BEC with the parameters taken as $\gamma = 1$, $N = 4 \times 10^6$, $a = 100 a_B$, and $(\omega_\perp, \omega_z) = 2\pi \times (100, 800)$ Hz. Then the stationary state is split in two components with opposite polarization as $\Psi_1 = \Psi_2 = \Psi_0/\sqrt{2}$. During the real-time evolution of the two components, we take $\gamma = 1$, $a_{11} = a_{22} = a_{12} = 100 a_B$, $(\omega_\perp, \omega_z) = 2\pi \times (100, 800)$ Hz, and $N_1 = N_2 = 2 \times 10^6$.

The results of the dynamic density modulation in a two-component dipolar BEC are shown in Fig. 5. At the initial time, the phase separation is induced by the DDI, which leads to the complicated domain structure with large kinetic energy [Fig. 5(b)]. Then the kinetic energy decays, while the dipolar domains of the system grow [Figs. 5(b) – 5(e)]. The domain structure is gradually rearranged [Figs. 5(e) – 5(g)]. A movie [42] shows the full evolution of the domain dynamics. The result herein is an analogy to the recent result of hydrodynamics in the magnetic domains of a spin-1 ferromagnetic BEC [43].

For thoroughly understanding the domain dynamics, we now perform analytical estimations of the characteristic lengths both at the beginning and at the longer time of the dipolar domain formation in 2D approximation.

At the beginning of the formation of the dipolar domains, the characteristic lengths are estimated by using Bogoliubov analysis of a uniform system. We define $g_{11}^{2D} = g_{22}^{2D} = g$, and write the wave functions as

$$\psi_i = e^{-iMt/\hbar}\left[\sqrt{n/2} + u_i e^{i\boldsymbol{k}\cdot\boldsymbol{\rho}} e^{-i\Omega t} + v_i^* e^{-i\boldsymbol{k}\cdot\boldsymbol{\rho}} e^{i\Omega^* t}\right], \tag{24}$$

where n is the 2D total density and $M = n(g + g_{12})/2$. Substituting Eq. (24) into Eq. (5) and diagonalizing the Bogoliubov

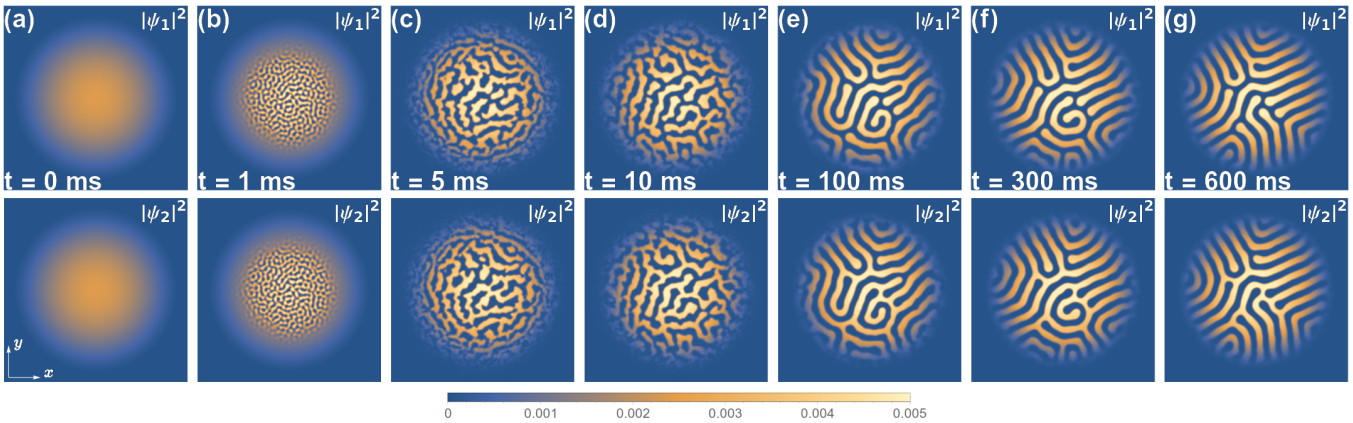

FIG. 5. (Color online) Column density profiles $|\psi_1|^2 = \int |\Psi_1|^2 dz$ and $|\psi_2|^2 = \int |\Psi_2|^2 dz$ for dynamical states with different time, in which components 1 and 2 have magnetic dipole moments $6\mu_B$ and $-6\mu_B$, respectively. $a_{11} = a_{22} = a_{12} = 100a_B$, $(\omega_\perp, \omega_z) = 2\pi \times (100, 800)$ Hz, $\gamma = 1$, and $N_1 = N_2 = 2 \times 10^6$. (a) - (f): $t = 0$, 1, 5, 10, 100, 300, 600 ms, respectively. The top row is for component 1, while the bottom row is for component 2. The field of view is 56×56 μm. See Supplemental Material for the movie of the dynamics [42].

matrix, we obtain

$$\hbar\Omega = \sqrt{\epsilon_k \left[\epsilon_k + (g + g_{12})\, n\right]}, \tag{25}$$

$$\hbar\Omega = \sqrt{\epsilon_k \left\{\epsilon_k + 2\left[g - g_{12} + 2g_{dd}\, h\,(q)\right] n\right\}}, \tag{26}$$

where $\epsilon_k = \hbar^2 k^2/(2m)$. Eqs. (25) and (26) correspond to the eigenfrequencies of the density and spin waves, respectively. Eq. (26) indicates that the phase separation can occur due to the DDI even when the two components are miscible ($g > g_{12}$) without DDI. We further assume $g_{12}^{2D} = g$, and use the expansion of the dipolar kernel as

$$h\,(q) = 2 - 3\left[1 - \frac{1}{2}q^{-2} + O\left(q^{-4}\right)\right], \tag{27}$$

then Eq. (26) can be approximately rewritten as

$$\Omega^2 \simeq \frac{1}{4m}\left[\frac{\hbar^2 k^4}{m} + 8g_{dd}n\left(-k^2 + 3\zeta^{-2}\right)\right]. \tag{28}$$

The system is therefore dynamically unstable for

$$g_{dd}n \gtrsim \frac{3\hbar^2}{2m\zeta^2}, \tag{29}$$

and the most unstable wave number k_u is

$$k_u \simeq \frac{2\sqrt{mg_{dd}n}}{\hbar}, \tag{30}$$

which corresponds to the characteristic wave number in the phase separation at the beginning of the time evolution as shown in Fig. 5(b).

At the longer time, for the case with striped labyrinthine pattern in Fig. 5(g), we apply the trial wave functions as the following forms

$$\psi_1 = \sqrt{n}\sqrt{\frac{1 + \cos K\rho}{2}}, \tag{31}$$

$$\psi_2 = \sqrt{n}\sqrt{\frac{1 - \cos K\rho}{2}}, \tag{32}$$

then the total energy becomes

$$\frac{E}{N} = \frac{\hbar^2 K^2}{8m} + \frac{g_{dd}n}{4}h\left(K\zeta/\sqrt{2}\right) \simeq \frac{\hbar^2 K^2}{8m} + \frac{g_{dd}n}{4}\left(-1 + 3K^{-2}\zeta^{-2}\right), \tag{33}$$

in which the s-wave interaction energy is independent of K and neglected. Then the wave number K minimizing the energy is

$$K = \frac{(6mg_{dd}n)^{1/4}}{\sqrt{\hbar\zeta}}. \tag{34}$$

Substituting the parameters used in Fig. 5 into Eqs. (30) and (34), the characteristic domain size at initial time is estimated to be $2\pi/k_u \simeq a_\perp$, while that at longer time is $2\pi/K \simeq 2a_\perp$ with $a_\perp = \sqrt{\hbar/m\omega_\perp}$. This analytical result is in qualitative agreement with the domain patterns in the dynamic simulations shown in Fig. 5.

IV. DOMAIN PATTERNS IN STATIONARY STATES

A. Number Ratio

Using imaginary-time propagation, we investigate the stationary states with different numbers of atoms N_2 in component 2 with fixed N_1 in component 1. We take $a_{11} = a_{22} = a_{12} = 100a_B$, and $(\omega_\perp, \omega_z) = 2\pi \times (100, 800)$ Hz. The number of atoms in component 1 is fixed to $N_1 = 2 \times 10^6$, while the number of atoms in component 2, N_2, is varied. In all the following simulations, the dipolar strength coefficient $\gamma = 1$ is maintained. The ratio between the numbers of atoms N_1/N_2 is changed from 1 to 10.

The column density profiles are plotted in Fig. 6. Phase separation shown in Fig. 6(a) arises from the opposite polarization of dipole moments in the two components, and rotational symmetry breaking (labyrinthine pattern) appears spontaneously due to the strong dipolar interactions. Moreover, it is shown

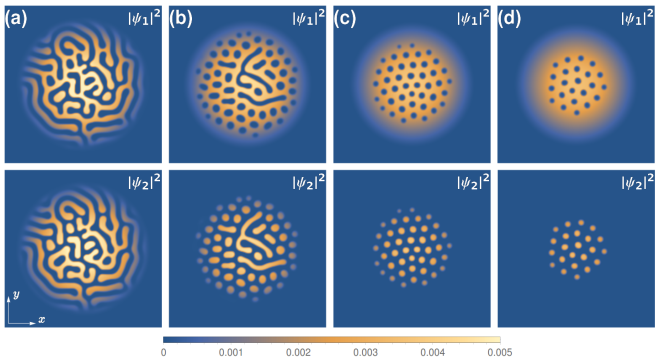

FIG. 6. (Color online) Column density profiles $|\psi_1|^2 = \int |\Psi_1|^2 dz$ and $|\psi_2|^2 = \int |\Psi_2|^2 dz$ for stationary states with fixed N_1 and changing N_2, in which components 1 and 2 have magnetic dipole moments $6\mu_B$ and $-6\mu_B$, respectively. $\gamma = 1$, $a_{11} = a_{22} = a_{12} = 100a_B$, and $(\omega_\perp, \omega_z) = 2\pi \times (100, 800)$ Hz. $N_1 = 2 \times 10^6$. (a) - (d): $N_1/N_2 = 1$, 2, 5, 10, respectively. The top row is for component 1, while the bottom row is for component 2. The field of view is 56×56 μm.

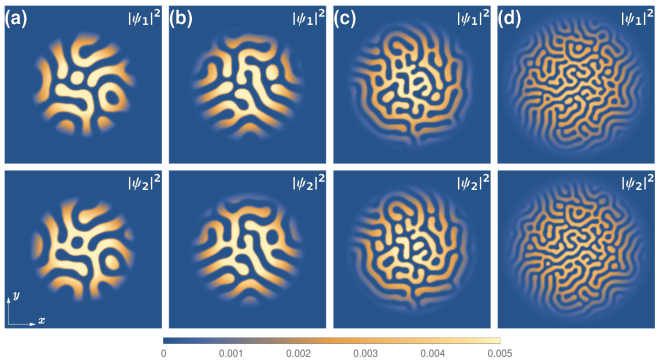

FIG. 7. (Color online) Column density profiles $|\psi_1|^2 = \int |\Psi_1|^2 dz$ and $|\psi_2|^2 = \int |\Psi_2|^2 dz$ for stationary states with different trap ratios, in which components 1 and 2 have magnetic dipole moments $6\mu_B$ and $-6\mu_B$, respectively. $\gamma = 1$, $a_{11} = a_{22} = a_{12} = 100a_B$, and $N_1 = N_2 = 2 \times 10^6$. $\omega_\perp = 2\pi \times 100$ Hz, (a) - (d): $\lambda = 1$, 4, 8, and 16, respectively. The top row is for component 1, while the bottom row is for component 2. The field of view is 56×56 μm.

that droplet pattern occurs when $N_1/N_2 > 1$, in which the droplets tend to form a triangular lattice. The crystallization of the dipolar droplets is similar to that observed in Ref. [21]. The number of droplets decreases as N_2 is decreased. For component 2 (bottom row in Fig. 6) with smaller number of atoms, filament structure splits into droplets and tends to assemble toward the center as the effective repulsion of component 1 is augmented with increasing the number ratio N_1/N_2.

B. Trap Ratio

We then investigate the trap geometry effect on the pattern formation in the two-component dipolar BEC. The number of atoms in the two components are kept the same, i.e., $N_1 = N_2 = 2 \times 10^6$, and $a_{11} = a_{22} = a_{12} = 100a_B$ are taken. The radial trap frequency is fixed as $\omega_\perp = 2\pi \times 100$ Hz, while the

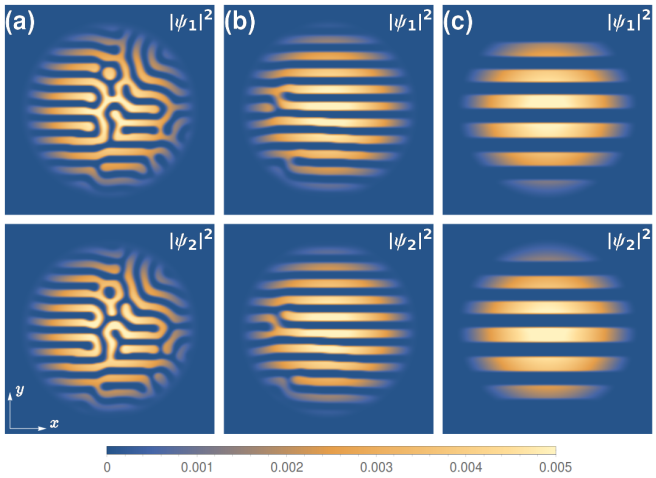

FIG. 8. (Color online) Column density profiles $|\psi_1|^2 = \int |\Psi_1|^2 dz$ and $|\psi_2|^2 = \int |\Psi_2|^2 dz$ for stationary states with different tilted angles α, in which components 1 and 2 have magnetic dipole moments $6\mu_B$ and $-6\mu_B$, respectively. $\gamma = 1$, $a_{11} = a_{22} = a_{12} = 100a_B$, $(\omega_\perp, \omega_z) = 2\pi \times (100, 800)$ Hz, and $N_1 = N_2 = 2 \times 10^6$. (a) - (c): $\alpha = \pi/12$, $\pi/6$, $\pi/3$, respectively. The top row is for component 1, while the bottom row is for component 2. The field of view is 56×56 μm.

trap ratio defined by $\lambda = \omega_z/\omega_\perp$ is changed from 1 to 16.

The column density profiles with $\lambda = 1$, 4, 8 and 16 are plotted in Fig. 7. As the trap ratio increases with fixed radial trap potential, the axial trap potential is enhanced, which gives rise to the phenomenon that the peaks of column density profiles in both components become lower. The atoms in the trap tend to be expanded towards outside along the radial directions, since the density increases with an increase in the axial confinement. Thus, more complicated labyrinthine pattern is formed for larger λ with radial trap frequency being fixed. The decrease in the domain size with an increase in λ can also be understood from Eq. (34), since the width ζ in the z direction decreases with an increase in λ. The pattern in Fig. 7(c) is the same as that in Fig. 6(a) due to the same parameter settings.

C. Tilted Polarization

The effect of a tilted polarization on the 2D dipolar Bose gas has recently been studied by mean-field theory [39] and dynamic many-body theory [44]. We now investigate the effect of tilted polarization on the interface of a three-dimensional two-component dipolar BEC system. The parameters are taken to be $a_{11} = a_{22} = a_{12} = 100a_B$, $(\omega_\perp, \omega_z) = 2\pi \times (100, 800)$ Hz, and $N_1 = N_2 = 2 \times 10^6$. The angle α of tilted polarization with respect to z direction is increased from $\pi/12$ to $\pi/3$.

We plot the column density profiles in Fig. 8. The results with $\alpha = \pi/12$, $\pi/6$, and $\pi/3$ are shown. As the tilted angle α increases, the filaments of labyrinthine structure in Fig. 6(a) are straightened gradually, and the labyrinthine pattern is reorganized into stripe phase as shown in Fig. 8(c), which is similar to the quantum phase transition in the 2D case in Ref.

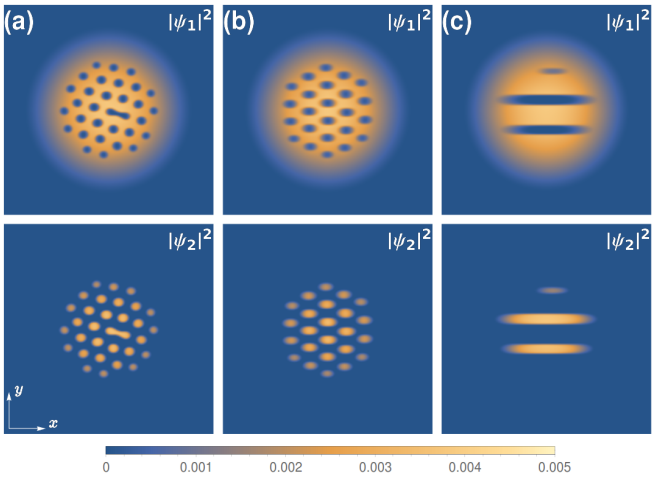

FIG. 9. (Color online) Column density profiles $|\psi_1|^2 = \int |\Psi_1|^2 dz$ and $|\psi_2|^2 = \int |\Psi_2|^2 dz$ for stationary states with different tilted angles α, in which components 1 and 2 have magnetic dipole moments $6\mu_B$ and $-6\mu_B$, respectively. $\gamma = 1$, $a_{11} = a_{22} = a_{12} = 100a_B$, $(\omega_\perp, \omega_z) = 2\pi \times (100, 800)$ Hz, and $N_1 = 2 \times 10^6$, $N_1/N_2 = 6$. (a) - (c): $\alpha = \pi/12, \pi/6, \pi/3$, respectively. The top row is for component 1, while the bottom row is for component 2. The field of view is 56×56 μm.

[44]. It is shown that the tilted polarization overcomes the effect of labyrinthine instability, and develops ordered stripe pattern replacing the disordered labyrinthine pattern.

We then change the number ratio of atoms in the two components as $N_1/N_2 = 6$. The column density profiles are plotted in Fig. 9 with $\alpha = \pi/12$, $\pi/6$ and $\pi/3$ as well. The droplet pattern induced by the large number ratio is also reshaped into stripe pattern as the tilted polarization angle increases. It is shown that crystallized droplet pattern occurs when $\alpha = \pi/6$ and $N_1/N_2 = 6$. Comparing Fig. 9(c) with Fig. 8(c), we find that the stripe phase transition is dwindled down as the atomic density decreases.

V. CONCLUSIONS

In conclusion, we have investigated the pattern formation of fingering instabilities and domain dynamics in an oppositely polarized two-component BEC with strong dipole-dipole interactions in three dimensions.

We have demonstrated dynamical fingering instabilities occurring at the interface between two components of dipolar BECs. Frog-shaped and mushroom-shaped patterns have been shown with different strengths of the dipolar interactions. The corresponding Bogoliubov analyses have also been performed for deeper understanding of the interfacial instabilities of the two dipolar BECs, and the dispersion relation similar to that in the classical fluids is analyzed. Spontaneous density modulation and dipolar domain growth in the dynamics have been demonstrated as well, in which we have analyzed the characteristic sizes of the dipolar domains corresponding to different patterns at the initial and longer time in the evolution. The rotational symmetry breaking arising from fingering instability spontaneously occurs at the interface, and develops droplet patterns due to the population imbalance in two components, labyrinthine patterns growing as the trap ratio increases, stripe phases as the angle of tilted polarization enlarges.

The anisotropy and long-range nature of dipole-dipole interactions have triggered various novel phenomena, which show similarities to that conventionally arising from viscosity in the classical fluids and shed new light on the nature of dipolar BECs, so we expect these phenomena to be observed in the experiments in the near future. Recently, a numerical study on superfluid flow over a rough surface of a wire shows similar properties of boundary layer to that in classical fluids [45], which also establishes stronger ties between superfluids and classical fluids than one has thought before.

ACKNOWLEDGMENTS

K.-T.X. would like to thank E. Braaten for his kind support and comments. T.B. acknowledges support by the Shanghai Research Challenge Fund, New York University Global Seed Grants for Collaborative Research, National Natural Science Foundation of China (Grant No. 61571301), the Thousand Talents Program for Distinguished Young Scholars (Grant No. D1210036A), and the NSFC Research Fund for International Young Scientists (Grant No. 11650110425). H.S. acknowledges support by JSPS KAKENHI Grants No. JP17K05595, No. JP16K05505, No. JP17K05596, No. JP26400414, and No. JP25103007.

[1] D. Bensimon, L. P. Kadanoff, S. Liang, B. I. Shraiman, and C. Tang, Rev. Mod. Phys. **58**, 977 (1986).
[2] R. V. Craster and O. K. Matar, Rev. Mod. Phys. **81**, 1131 (2009).
[3] L. Keiser, H. Bense, P. Colinet, J. Bico, and E. Reyssat, Phys. Rev. Lett. **118**, 074504 (2017).
[4] D. Pihler-Puzović, P. Illien, M. Heil, and A. Juel, Phys. Rev. Lett. **108**, 074502 (2012).
[5] Z. Zheng, H. Kim, and H. A. Stone, Phys. Rev. Lett. **115**, 174501 (2015).
[6] J. Kim, F. Xu, and S. Lee, Phys. Rev. Lett. **118**, 074501 (2017).
[7] W. Mather, O. Mondragón-Palomino, T. Danino, J. Hasty, and L. S. Tsimring, Phys. Rev. Lett. **104**, 208101 (2010).
[8] D. D. Ryutov, M. S. Derzon, and M. K. Matzen, Rev. Mod. Phys. **72**, 167 (2000).
[9] P. W. Terry, Rev. Mod. Phys. 72, **109** (2000).
[10] S. E. Woosley, A. Heger, and T. A. Weaver, Rev. Mod. Phys. **74**, 1015 (2002).
[11] A. Burrows, Rev. Mod. Phys. **85**, 245 (2013).
[12] J. J. Hester, Annu. Rev. Astron. Astrophys. **46**, 127 (2008).
[13] L. Romankiw, M. Slusarczuk, and D. Thompson, IEEE Trans.

Magn. **11**, 25 (1975).
[14] D. P. Jackson, R. E. Goldstein, and A. O. Cebers, Phys. Rev. E **50**, 298 (1994).
[15] K. Sasaki, N. Suzuki, D. Akamatsu, and H. Saito, Phys. Rev. A **80**, 063611 (2009).
[16] S. Gautam and D. Angom, Phys. Rev. A **81**, 053616 (2010).
[17] A. Bezett, V. Bychkov, E. Lundh, D. Kobyakov, and M. Marklund, Phys. Rev. A **82**, 043608 (2010).
[18] D. Kobyakov, V. Bychkov, E. Lundh, A. Bezett, V. Akkerman, and M. Marklund, Phys. Rev. A **83**, 043623 (2011).
[19] T. Kadokura, T. Aioi, K. Sasaki, T. Kishimoto, and H. Saito, Phys. Rev. A **85**, 013602 (2012).
[20] H. Saito, Y. Kawaguchi, and M. Ueda, Phys. Rev. Lett. **102**, 230403 (2009).
[21] H. Kadau, M. Schmitt, M. Wenzel, C. Wink, T. Maier, I. Ferrier-Barbut, and T. Pfau, Nature **530**, 194 (2016).
[22] M. Schmitt, M. Wenzel, F. Böttcher, I. Ferrier-Barbut, and T. Pfau, Nature **539**, 259 (2016).
[23] I. Ferrier-Barbut, H. Kadau, M. Schmitt, M. Wenzel, and T. Pfau, Phys. Rev. Lett. **116**, 215301 (2016).
[24] K.-T. Xi and H. Saito, Phys. Rev. A **93**, 011604(R) (2016).
[25] R. N. Bisset and P. B. Blakie, Phys. Rev. A **92**, 061603(R) (2015).
[26] P. B. Blakie, Phys. Rev. A **93**, 033644 (2016).
[27] H. Saito, J. Phys. Soc. Jpn. **85**, 053001 (2016).
[28] F. Wächtler and L. Santos, Phys. Rev. A **93**, 061603(R) (2016).
[29] F. Wächtler and L. Santos, Phys. Rev. A **94**, 043618 (2016).
[30] R. N. Bisset, R. M. Wilson, D. Baillie, and P. B. Blakie, Phys. Rev. A **94**, 033619 (2016).
[31] D. Baillie, R. M. Wilson, R. N. Bisset, and P. B. Blakie, Phys. Rev. A **94**, 021602(R) (2016).
[32] A. Griesmaier, J. Werner, S. Hensler, J. Stuhler, and T. Pfau, Phys. Rev. Lett. **94**, 160401 (2005).
[33] L. Santos and T. Pfau, Phys. Rev. Lett. **96**, 190404 (2006).
[34] T. Lahaye, T. Koch, B. Frohlich, M. Fattori, J. Metz, A. Griesmaier, S. Giovanazzi, and T. Pfau, Nature **448**, 672 (2007).
[35] S. Giovanazzi, A. Görlitz, and T. Pfau, Phys. Rev. Lett. **89**, 130401 (2002).
[36] See Supplemental Material for the movie of the time evolution of the column densities of two components with $\gamma = 0.18$.
[37] See Supplemental Material for the movie of the time evolution of the column densities of two components with $\gamma = 1$.
[38] See Supplemental Material for the movie of the time evolution of the column densities of two components with $\gamma = 0$.
[39] C. Ticknor, R. M. Wilson, and J. L. Bohn, Phys. Rev. Lett. **106**, 065301 (2011).
[40] S. Chandrasekhar, *Hydrodynamic and hydromagnetic stability*, (Clarendon Press, Oxford, 1961) Chap. 10.
[41] B. Van Schaeybroeck, Phys. Rev. A **78**, 023624 (2008); Phys. Rev. A **80**, 065601 (2009).
[42] See Supplemental Material for a movie of the domain dynamics.
[43] K. Kudo and Y. Kawaguchi, Phys. Rev. A **84**, 043607 (2011).
[44] A. Macia, D. Hufnagl, F. Mazzanti, J. Boronat, and R. E. Zillich, Phys. Rev. Lett. **109**, 235307 (2012).
[45] G. W. Stagg, N. G. Parker, and C. F. Barenghi, Phys. Rev. Lett. **118**, 135301 (2017).